ACS APPLIED MATERIALS & INTERFACES

Research Article

www.acsami.org

Double-Sided Brush-Shaped TiO_2 Nanostructure Assemblies with Highly Ordered Nanowires for Dye-Sensitized Solar Cells

Chenyang Zha,[†] Liming Shen,[†] Xiaoyan Zhang,[†] Yifeng Wang,[†] Brian A. Korgel,[‡] Arunava Gupta,[§] and Ningzhong Bao*,[†]

[†]State Key Laboratory of Materials-Oriented Chemical Engineering, College of Chemistry and Chemical Engineering, Nanjing University of Technology, Jiangsu, Nanjing 210009, P. R. China

[‡]Department of Chemical Engineering, Texas Materials Institute, Center for Nano- and Molecular Science and Technology, The University of Texas at Austin, Austin, Texas 78712-1062, United States

[§]Center for Materials for Information Technology (MINT), The University of Alabama, Tuscaloosa, Alabama 35487, United States

Supporting Information

ABSTRACT: We describe a seeded hydrothermal process for the growth of unique double-sided brush-shaped (DSBS) TiO_2 nanostructure assemblies consisting of highly ordered rutile nanowires vertically aligned around an annealed TiO_2 nanoparticle layer. The annealed TiO_2 nanoparticle layer seeds the nanowire growth and also supports the DSBS structure. The morphology of the DSBS TiO_2 nanostructure depends on the hydrothermal reaction time. The diameter of the nanowires is about 6.6 nm, and with increasing reaction time from 1 to 8 h the nanowire length increases from 0.6 to 6.2 μm, whereas the thickness of the nanoparticle layer decreases from 4.3 to 2.8 μm. These free-standing nanowire arrays provide large internal surface area, which is essential for minimizing carrier recombination in high performance photovoltaic devices. Furthermore, the nanowire architecture can help increase the rate of charge transport as compared to particulate films because of lower concentration of grain boundaries. The power conversion efficiency of backside (DSBS TiO_2/FTO photoanode) illuminated dye-sensitized solar cells fabricated using the DSBS TiO_2 nanostructure assembly is found to be depended on the nanowire length. A cell fabricated using 15.2 μm thick nanostructures sensitized by N719 has a short-circuit current density of 12.18 mA cm^{-2}, 0.78 V open circuit potential, and a 0.59 filling factor, yielding a maximum power conversion efficiency of 5.61% under AM 1.5 illumination.

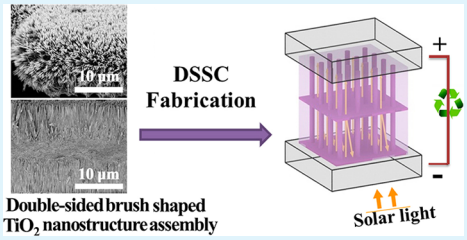

KEYWORDS: *TiO_2, nanostructure, nanowire arrays, hydrothermal synthesis, dye-sensitized solar cells*

INTRODUCTION

Since the significant breakthrough in the device efficiency of dye-sensitized solar cells (DSSCs) achieved by Michael Gratzel and his collaborators,[1] DSSC has been considered as one of the most promising solutions for addressing global fossil fuel depletion and environmental pollution problems.[2] A typical DSSC consists of a photoanode, dye, electrolyte, and a photocathode. In such a device structure, a sensitizer as light-absorbing material is coupled with a wide bandgap nanocrystalline semiconductor, to realize efficient optical absorption and charge separation.[3] Nanostructured TiO_2 is one of the most important photoelectrode material and has been widely investigated for use in DSSCs.[4] A variety of TiO_2 nanomaterials with different morphologies, such as nanoparticles, nanotubes, nanorods, nanowires, and nanosheets, etc., have been prepared for fabrication of DSSCs, with the morphology of TiO_2 nanomaterials having a significantly influence on the conversation efficiency of fabricated solar cells.[5−13] In general, high specific surface area, efficient electron diffusion pathway, and pronounced light-trapping are indispensable for a high-performance photoanode in DSSCs.[14] However, these criteria are often incompatible with one another.[15] To date, the highest efficiency DSSC devices have used porous TiO_2 nanoparticle films, with maximum cell efficiencies of 12.3% using a liquid electrolyte[16] and 15.4% with solid state electrolyte.[17,18] Porous TiO_2 nanoparticle networks offer high internal surface area for anchoring a large quantity of dye for maximizing light harvesting, thereby enhancing the generation of photo-induced carriers.[19] Nevertheless, disorder in porous nanoparticulate networks can result in poor electronic transport with increased carrier recombination.

One-dimensional high-ordered nanoarchitectures with improved electron transport properties can increase the efficiency of dye-sensitized solar cells.[20] Such nanoarchitectures in the form of nanotubes, nanorods, and nanowires have been suggested as better scaffolds for DSSCs, with lower carrier recombination and more efficient electron transport.[5−7] The enhanced efficiency of electron diffusion, attributed to direct electron transport, was clearly demonstrated for vertically-aligned TiO_2 nanotubes prepared by solution electrochemical

Received: July 30, 2013
Accepted: December 12, 2013
Published: December 12, 2013

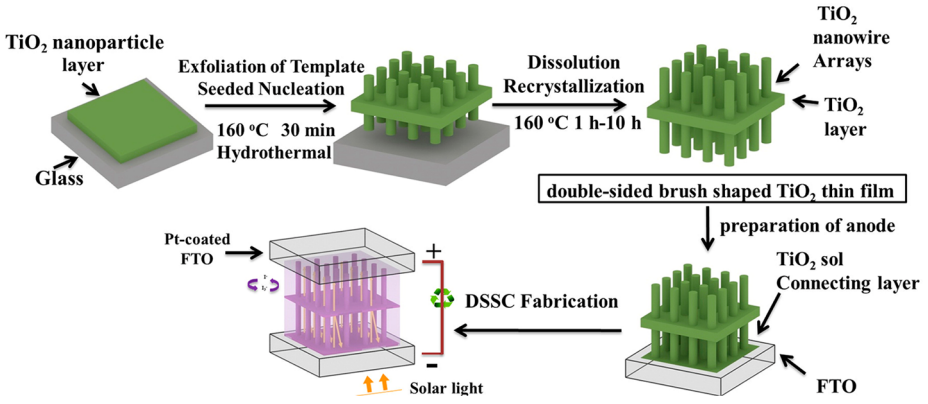

Figure 1. Schematic illustration of the synthetic procedure of DSBS TiO_2 thin films and fabrication of DSSCs.

anodic oxidation of Ti metal plates or Ti films sputter coating on TCO glass slides.[5] Besides TiO_2 nanotube arrays, 1D single-crystalline TiO_2 nanowire/nanorod arrays have also been widely studied for DSSCs. The electron transport in crystalline wires is expected to be several orders of magnitude faster than percolation through a random polycrystalline network. Hydrothermal synthesis provides an effective approach for growth of novel nanowires/nanorods used as photoanodes.[21−24] Kakiuchi et al. prepared rutile TiO_2 rods on silica glass substrates by hydrothermal reaction at temperatures of 80 and 200 °C.[25] Feng et al. reported the hydrothermal growth of TiO_2 nanorod arrays on FTO glass substrates and used them to fabricate DSSCs with power conversion efficiency of 3.74%.[26] Liu et al. developed a facile hydrothermal method to grow oriented single-crystalline rutile TiO_2 nanorod layers on FTO substrates and a 3% power conversion efficiency was achieved using 4 μm-long TiO_2 nanorod structure as the photoanode in a DSSC.[7] Recently, DSSCs fabricated using TiO_2 nanostructures consisting of 1D nanowire arrays at the bottom and a 3D dendritic microsphere on the top layer achieved 7.2% power conversion efficiency.[27] Nevertheless, large size and dense packing of 1D nanowires and/or nanorods can significantly lower the exposed surface area, resulting in reduced dye adsorption.

Overall, the assembly of hierarchical nanostructures of 1D nanowire arrays has attracted wide attention because of their desirable characteristics such as special nano-topography, hierarchical internal nanostructure, and multiphase anisotropic interfaces. These hierarchical nanostructures are expected to greatly enhance the performance of dye-sensitized solar cells.[28] In this work, we report on a facile process for hydrothermal growth of unique double-sided brush-shaped (DSBS) TiO_2 nanostructure assemblies consisting of highly ordered TiO_2 nanowires vertically aligned around an annealed TiO_2 nanoparticle layer. The annealed TiO_2 nanoparticle layer seeds the nanowire growth and maintains the structural integrity of the DSBS structure. This novel DSBS structure, with highly ordered free-standing TiO_2 nanowires, can provide larger internal space and surface area as compared to a single layer of TiO_2 nanowire arrays, which is beneficial for dye adsorption. Backside (DSBS TiO_2/FTO photoanode) illuminated DSSCs have been fabricated and tested using the DSBS TiO_2 nanostructure assembly. The device performance is found to be influenced by the length of TiO_2 nanowires.

EXPERIMENTAL SECTION

Synthesis of DSBS TiO_2 Nanostructure Assemblies. Figure 1 provides a schematic illustration of the synthetic procedure of DSBS TiO_2 nanostructure assembly and fabrication of the DSSC device. The first step was to prepare a TiO_2 nanoparticle layer using TiO_2 nanoparticle paste. The paste was prepared by dispersing TiO_2 nanoparticle powder (Degussa P25) into a solvent mixture of ethanol, ethyl cellulose, and terpineol, followed by grinding the paste in an agate mortar at room temperature for 30 min. A layer of TiO_2 paste with 4−5 μm thickness was coated onto a glass slide by doctor-printing method, dried at 80 °C for 30 min,[29] and then annealed at 400 °C for 60 min in air to form a TiO_2 nanoparticle layer, as seen Figure S1 in the Supporting Information. The second step was hydrothermal growth of the DSBS TiO_2 nanostrucure assembly. The obtained TiO_2 nanoparticle layer (2 cm ×2 cm) was immersed into a 15 ml reaction solution ($[H^+]$ = ~8.8 M) , consisting of a mixture of 1 ml titanium(IV) butoxide, 11 ml hydrochloric acid (38 wt %), and 4 mL of H_2O, in a 30 mL of Teflon-lined stainless steel autoclave. After adequate sealing, the autoclave was heated to 160 °C and maintained at this temperature for different reaction times from 30 min up to 10 h. The TiO_2 nanoparticle layer was found to separate from the glass slide within 30 min reaction time, which is critical to the formation of the DSBS structure because nanowires grow underneath the nanoparticle layer as well. The DSBS TiO_2 nanostructures were washed three times with deionized water and then in ethanol, and dried at 80 °C for 20 min.

Fabrication of DSSCs. The synthesized DSBS TiO_2 nanostructures were cut into 0.5 cm × 0.5 cm pieces. To prepare the DSSC anode, a DSBS nanostructure assembly was glued on to a FTO glass slide using a drop of TiO_2 sol as adhesive, and then annealed at 400 °C for 1 h in air.[30] The prepared anode was then soaked in 40 mM $TiCl_4$ aqueous solution for 30 min at 70 °C, dried at 80 °C for 20 min, and then annealed at 400 °C for 30 min in air and transferred into a N_2-filled glove box for dye absorption. The dye solution was prepared by dissolving 0.3 mM dye N719 in methanol. The dye absorption on the anode was performed by overnight soaking the electrode in the dye solution at 30 °C and then rinsed with pure ethanol to remove excess physically adsorbed dye molecules. In the fabricated DSSC, the dye-adsorbed DSBS TiO_2 nanostructure functioned as a photoanode, Pt-coated FTO glass slide functioned as a counter electrode. The assembly was sealed in a 25 mm thick hot melt gasket made of ionomer Surlyn 1702 (Dupont), and the electrolyte was introduced into the cell from a drilled hole on the counter electrode. The electrolyte solution was a mixture of 0.6 M 1-butyl-3-methyl imidazolium iodide, 0.03 M I_2, 0.10 M guanidinium thiocyanate, and 0.5 M 4-tertbutylpyridine in a mixture of acetonitrile and valeronitrile (85/15, v/v).

Materials Characterization. The crystal structure of the nanostructures and layers was characterized using XRD (X-ray diffractometer, Rigaku-Smart Lab Advance). Cu−Kα radiation (λ = 1.5408 Å) was used as the X-ray source, operating at 40 kV and 100

dx.doi.org/10.1021/am404942n | ACS Appl. Mater. Interfaces 2014, 6, 122−129

mA. All the samples were characterized in 2θ range of 20−80°, with a scan-speed 0.8 s/step and step increment of 0.02°/s. The morphology and microstructure of samples was characterized by optical microscopy, field-emission scanning electron microscopy (FESEM, HITACHI S−4800) equipped with energy- dispersive X-ray spectroscopy (EDS). High-resolution transmission electron microscopy (TEM, JEOL JEM−2100) coupled with selected area electron diffraction (SAED) was used to investigate the crystallinity and microstructure details of the samples, operating at 200 kV. The Raman spectra of the samples were measured using a commercial Raman spectrometer (Horiba Labram HR 800). A 514 nm He−Cd laser was used for excitation. The laser power on the sample surface was 20 mW. The scattered light was detected using a thermoelectrically cooled charge-coupled device. Surface area of the samples was determined from the amount of N_2 adsorption at 77 K. A Coulter Ominisorb 100cx, USA, was employed to obtain adsorption/desorption isotherms.

Performance of DSSCs. DSSC performance was characterized by measuring photocurrent density-voltage ($J-V$) curves under AM1.5 simulated solar light (100 mW cm^{-2}, Oriel 300 W Xe lamp, and Newport AM1.5 filter) over an active area of 0.2 cm^2. Incident photon-to-current efficiency (IPCE) spectra were recorded using an Oriel QE/IPCE Measurement Kit (equipped with 150−300 W full spectrum solar simulator). The electrochemical impedance spectroscopy (EIS) measurements were performed using an electrochemical workstation (AUTOLAB PGSTAT302N) under AM1.5 simulated solar light (100 mW cm^{-2}) in the frequency range of 0.1 Hz to 100 kHz, with the applied bias voltage and ac amplitude set at open-circuit voltage of the cells and 10 mV between the counter electrode and the working electrode, respectively.

RESULTS AND DISCUSSION

Material Structure and Properties. The microscopic characterization results of a DSBS TiO_2 nanostructure assembly with 8 h reaction time have been used to demonstrate the morphology and structure of the products. Figure 2a shows a top-view optical image of the DSBS TiO_2 nanostructure. No cracks are observed over the entire layer surface. Images b and c in Figure 2 show top-view and side-view FESEM images of the sample prepared under the same conditions. The entire surface is covered by well aligned nanowires. All of the nanowires are well-separated and free-standing, providing large internal space and surface area. The edges of the layer are also covered with the same high quality nanowires (Figure 2c). The cross-section SEM image of the sample (Figure 2d) shows that nanowire arrays with uniform sizes grow vertically around the central layer. Each individual nanowire has a sharp end (Figure 2e). The average diameter of the nanowires is measured to be around 6.6 nm. Figure 2f shows HRTEM image and SAED pattern (the inset) of a typical single TiO_2 nanowire. The SAED pattern confirms the single-crystalline nature of the nanowires. The lattice fringes can be clearly distinguished from the HRTEM image (the inset). The interplanar spacing is measured to be around 0.33 nm (corresponding to the rutile TiO_2 (110) planes), indicating preferential growth direction of rutile nanowires along the [001] direction. The result agrees with a previous report that the growth rate of different crystal faces in rutile TiO_2 nanowires in strong acidic solutions generally follows the order of (110) < (100) < (101) < (001).[31]

The formation process of the DSBS TiO_2 nanostructure assembly was investigated by examining the evolution of the morphology of the materials as they proceed through the reaction. Figure 3a−e shows cross-section SEM images of the products formed at hydrothermal reaction times of 1, 2, 4, 6, and 8 h, respectively. The TiO_2 nanoparticle layer was found separated from the supporting glass slide within 30 min reaction time. The initial growth of TiO_2 nanowires was

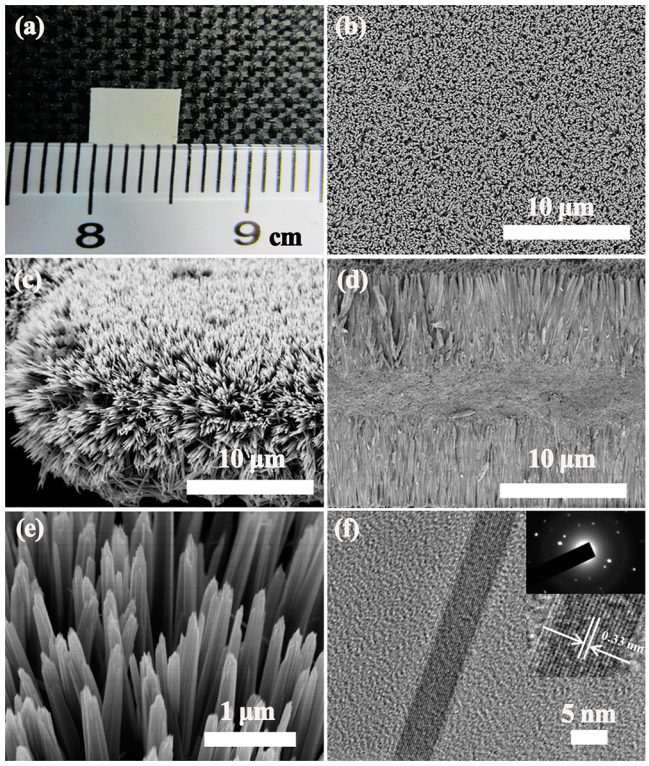

Figure 2. (a) Top-view optical image of a DSBS TiO_2 nanostructure formed after 8 h reaction time; (b) top-view, (c) side-view, and (d) cross-view FESEM images of the nanostructure prepared under the same conditions; (e) magnified FSEM image of the nanostructure showing well-separated and free-standing nanowires with sharp ends; (f) HRTEM image of an individual TiO_2 nanowire. The insets of f show SAED pattern (top) and HRTEM image (below) of the TiO_2 nanowire.

observed at 1 h, as seen in Figure 3a. All of the TiO_2 nanowires grew vertically around the central TiO_2 nanoparticle layer. The average nanowire length was around 0.3 μm. With longer reaction time, the length of nanowires increased significantly. As seen in Figure 3b−e, the length of nanowires formed at 2, 4, 6, and 8 h was measured to be 0.6, 2, 2.3, and 6.2 μm, respectively. Along with the growth of the nanowires, the thickness of the central TiO_2 layer gradually decreased from 4.3 μm at 2 h to 2.8 μm at 8 h. Figure 3f summarizes both the length change of nanowires and thickness change of the central TiO_2 nanoparticle layer with the hydrothermal reaction time. The thickness of the DSBS TiO_2 nanostructure assembly formed at 8 h reaction time was around 15.2 μm, very close to the optimized photoelectrode thickness for DSSCs fabricated based on P25 TiO_2 nanoparticles.[32,33] In reality, the optimum anode thickness of a DSSC depends on many factors, such as surface area, light confinement, extinction coefficient of the dye, charge transport properties of the network, etc.

The mechanical stability of TiO_2 nanostructure assemblies with highly ordered nanowires is determined by the thickness and structure of the central P25 TiO_2 layer. This is because along with the growth of the nanowires the anatase constituent of the annealed P25 TiO_2 layer gradually dissolved away and thus reduces the thickness of the center TiO_2 layer that acts as a support for the nanowires. The thickness of the center TiO_2 layer can be controlled by tuning the hydrothermal reaction time. The DSBS TiO_2 nanostructure assemblies formed within 8 h are sufficiently strong to withstand the latter procedure of

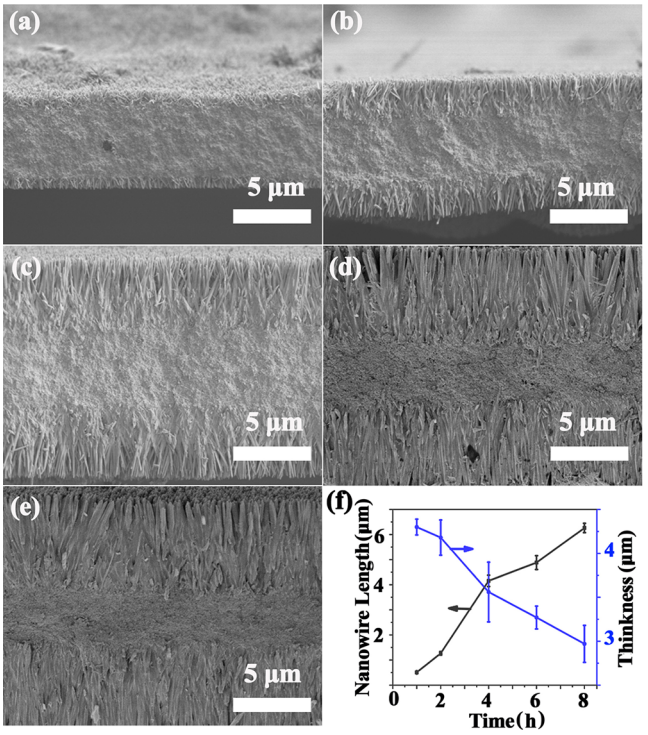

Figure 3. Cross-view SEM images of the samples formed at hydrothermal reaction time of (a) 1, (b) 2, (c) 4, (d) 6, and (e) 8 h. (f) The length of nanowires (left) and the thickness of TiO_2 nanoparticle film layer (right) as a function of the reaction time.

DSSC fabrication. However, TiO_2 layers formed beyond this time (such as after 10 h) are very fragile because they are too thin to sustain the DSBS structure.

The BET surface area of the typical 8 h DSBS TiO_2 nanostructure was calculated based on the N_2 adsorption/desorption isotherms (see Figure S2 in the Supporting Information) and is about 60 m^2/g, which is larger than for P25 TiO_2 nanoparticle powders (~50 m^2/g).

The crystallographic structure of the products obtained at different reaction times were identified by XRD analysis. The XRD pattern (Figure 4a) of the initial TiO_2 nanoparticle layer (Degussa P25 containing 80 wt % anatase and 20 wt % rutile) are well indexed to the standard XRD patterns of anatase

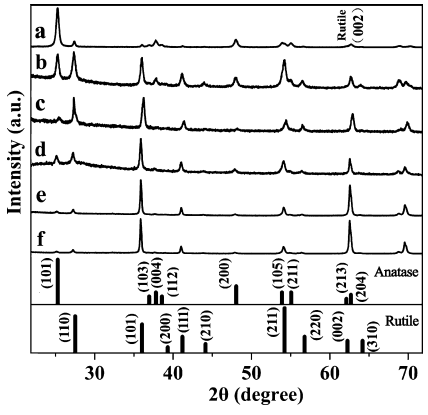

Figure 4. XRD patterns for (a) P25 nanoparticle powders and DSBS TiO_2 thin film formed at reaction time of (b) 1, (c) 2, (d) 4, (e) 6, and (f) 8 h. The standard XRD patterns of rutile (JCPDS No. 21-1272) and anatase (JCPDS No. 01-1292) are provided.

(JCPDS No. 21-1272) and rutile (JCPDS No. 01-1292). With reaction time increasing from 1 to 4 h, the intensity of characteristic peak (27°) of the product anatase phase (Figure 4b–f) decreased, while that of rutile phase increased. The rutile phase is dominant in the product after 6 h, as seen in spectra e and f in Figure 4. The decrease in intensity of anatase phase peak at 27° indicates that the phase transformation from anatase to rutile occurred during growth of the rutile nanowires. The strong peak of the rutile phase has contributions from both the nanowires and the starting TiO_2 layer. A remarkable increase in the intensity of the rutile phase (002) peak, along with a simultaneous decrease in the intensity of the rutile phase (110) peak, are observed in the XRD patterns from Figure 5b

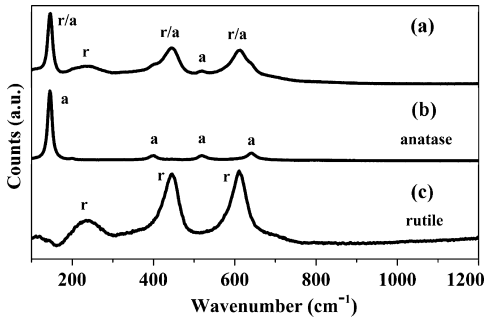

Figure 5. Raman spectra for (a) as-synthesized DSBS TiO_2 thin film after 8 h reaction time, and standard (b) anatase and (c) rutile powders purchased from Sigma. Symbols *r*, *a*, and *r*/*a* represents peaks of rutile, anatase, and the mixture of rutile and anatase, respectively.

to Figure 5f. Moreover, the rutile phase (101) peak of the nanowires formed at 1 h (Figure 5b) obviously gets stronger as compared to that for the original P25 nanoparticles (Figure 5a), but it then slowly increases in intensity with continued growth of the nanowires (Figure 5b–f) as there exists a ~32.8° angle between the rutile phase [101] and the [002] planes. Thus, the nanowires grow in the [001] direction, and the [110] crystal planes parallel to the c axis are exposed, as also suggested from the HRTEM and SAED results (Figure 2f inset).

The phase composition of the DSBS TiO_2 nanostructure assembly has been further studied using Raman spectroscopy. Figure 5 shows Raman spectra of the DSBS TiO_2 nanostructure produced after a reaction period of 8 h (Figure 5a), along with the spectra for standard anatase (Figure 5b) and rutile powder (Figure 5c). The standard anatase powder (Figure 5b) shows major Raman bands at 144, 399, 519, and 639 cm^{-1}, corresponding to four Raman-active modes of the anatase phase with symmetries of E_g, B_{1g}, B_{1g}, and E_g, respectively.[34] The typical Raman bands of the standard rutile phase (Figure 5b) appear at 143, 235, 447, and 612 cm^{-1}, which can be ascribed to the B_{1g}, two-phonon trapping, E_g, and A_{1g} modes of rutile phase, respectively.[35] The bands for the 8 h DSBS TiO_2 sample (Figure 5a) are consistent with those of anatase and rutile, confirming the co-existence of both phases.

Formation of DSBS TiO_2 Nanostructures. Three processes occur during the formation of DSBS TiO_2 nanostructures: (1) seeded hydrothermal nucleation of rutile nuclei; (2) oriented growth of rutile nanowires; and (3) dissolution of the TiO_2 nanoparticle layer. During the nucleation step, relatively slow hydrolysis of titanium(IV) butoxide under strong acidic condition ($[H^+] \approx 8.8$ M) causes the formation of octahedral $[Ti(OH)_2(OH)_2]^{2+}$ monomers.[36] Process conditions such as pH value of the sol-gel system,

dx.doi.org/10.1021/am404942n | ACS Appl. Mater. Interfaces 2014, 6, 122–129

catalyst concentration, calcination temperature, etc., have been found to be primary factors that can significantly affect the particle size, crystal phase, and nanostructure of the TiO_2 products.[37] As the concentration of the monomers increases to a critical value, they combine together through oxolation or olation, resulting in the nucleation of rutile nuclei on the TiO_2 nanoparticle layer. The HCl concentration determines the crystal phase of the TiO_2 products because rutile is the equilibrium phase under strongly acidic conditions.[38−40] After nucleation, nanowire growth in the [001] direction is promoted by the differing growth rates of the distinct crystal faces of the rutile structure. The anisotropic growth of (002) planes likely can be explained by facet-selective adsorption of Cl^- ions on the (110) crystal planes of rutile TiO_2 to suppress their growth.[6,25,31,41,42] With growth of the nanowires, the anatase constituent in the TiO_2 nanoparticle layer gradually dissolves, providing additional titanium for continued growth of the nanowires. As a result, the center TiO_2 layer decreases in thickness (Figure 3f) and there is reduced anatase content in the reaction products (Figure 4). Previous studies have shown that the sequential process of dissolution and recrystallization dominates the formation of titania under strong acidic hydrothermal conditions using insoluble solid TiO_2 and titanates as titanium precursors.[41] When the $[H^+]$ concentration is increased above 12 M under the same reaction conditions, nanowires are not formed. This is due to the high solubility of titanium under strong acidic conditions, consistent with our previous results.[39]

The anatase-to-rutile ratio decreases with dissolution of the anatase constitutient in the TiO_2 nanoparticle layer and hydrothermal growth of the rutile nanowires. To confirm the dissolution of TiO_2 nanoparticle layer (process 3), was conducted a control experiment without the addition of titanium(IV) butoxide. After 30 min reaction time, the anatase-to-rutile peak intensity ratio of the product decreased from the initial value of 5 (25° in XRD):1 (27° in XRD) (see Figure S3a in the Supportng Information) to 5 (25° in XRD) :2 (27° in XRD) (see Figure S3b in the Supporting Information), indicating that the anatase in the nanoparticle layer gradually dissolved in the solution (see Figure S4a, b in the Supporting Information). Because the octahedral $[Ti(OH)_2(OH_2)]^{2+}$ monomers formed solely through the dissolution of anatase in the TiO_2 nanoparticle layer, its low concentration likely caused a low recystallization rate of TiO_2 nanowires and a fast dissolution rate of the TiO_2 nanoparticle layer. Therefore, the TiO_2 nanoparticle layer completely collapsed within 1 h (see Figure S4c−e in the Supporting Information). Depending upon the reaction time, the resulting colloidal solution could exist either in the form of TiO_2 nanoparticle agglomerate suspensions (see Figure S5b, c in the Supporting Information) or stable clear colloids (see Figure S5d, e in the Supporting Information). For example, agglomerates were observed after 30 min reaction time (see Figure S5b in the Supporting Information). The shape and size of the agglomerates were significantly different from that of particles that remained on the TiO_2 layer (see Figure 4b in the Supporting Information). As seen in Figure S6 in the Supporting Information, the TiO_2 nanoparticles that remained on the glass slide after 30 min (see Figure S6a in the Supporting Information) showed a regular spherical shape and uniform size that are much larger than that of irregular fine particles in the TiO_2 agglomerates in solution (see Figure S6b in the Supporting Information). The result confirms that the continuous dissolution of the anatase phase in the TiO_2 nanoparticle layer provided the reactants for the growth of the nanowires. It also contributed to separation from the glass slide. The central porous nanoparticle layer of DSBS TiO_2 can not only help to retain the DSBS structure but also enhance the dye absorption, thus increasing light trapping.[14,32]

The reactants used for the growth of DSBS TiO_2 nanostructures on the TiO_2 nanoparticle layer is not restricted to titanium(IV) butoxide. Other titanium sources, such as titanium isopropoxide and titanium tetrachloride, also leads to the formation of DSBS TiO_2 nanostructure using the same synthetic procedure. As seen Figure S7a, b in the Supporting Information, the nanowires with flat ends are synthesized using titanium isopropoxide. If titanium tetrachloride is used as the titanium precursor, longer single side nanowires with lengths of 15 μm can be synthesized (see Figure S7c, d in the Supporting Information).

DSSC Performance. The *I*−*V* characteristics of the DSSC devices fabricated using DSBS TiO_2 nanostructure assemblies synthesized at reaction times of 4, 6, and 8 h and the annealed P25 particle film are shown in Figure 6a. Table 1 summarizes

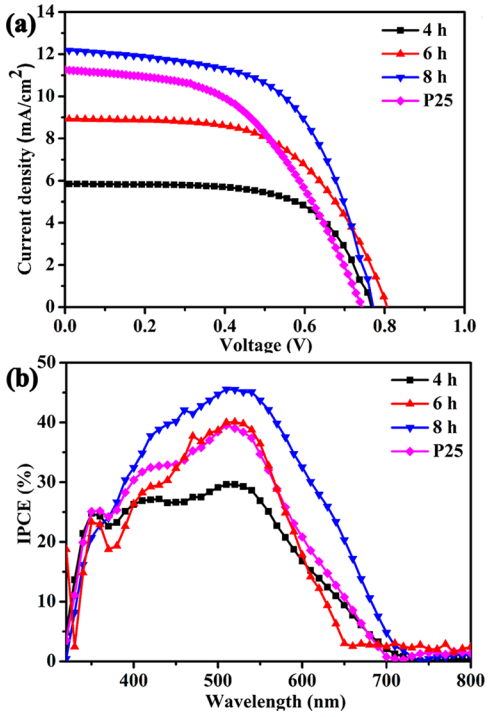

Figure 6. (a) Characteristic *I*−*V* curves and (b) IPCE spectra for DSSCs fabricated using DSBS TiO_2 thin films synthesized at different hydrothermal reaction times of 4, 6, and 8 h. The characteristics of a DSSC assembled using P25 particles as photoelectrode with similar thickness is also included. The active area of all four DSSCs is 0.25 cm^2.

the cell performance parameters for all four DSSCs. Under 100 mW cm^{-2} AM1.5 illumination, the cell fabricated using a 4 h DSBS TiO_2 nanostructure (4 μm-long nanowires and 3.5 μm thick central nanoparticle layer) had a 2.89% conversion efficiency (η) with J_{sc} = 5.85 mA cm^{-2} , V_{oc} = 0.76 V, and FF = 0.65. The cell fabricated using a 6 h reaction time DSBS TiO_2 (4.5 μm long nanowires and 3.3 μm thick central nanoparticle layer) provided η = 4.12%, with J_{sc} = 9.0 mA cm^{-2}, V_{oc} = 0.79 V, and FF = 0.58. The cell fabricated using a 8 h DSBS TiO_2 (6 μm long nanowires and 3 μm thick central nanoparticle layer)

dx.doi.org/10.1021/am404942n | ACS Appl. Mater. Interfaces 2014, 6, 122−129

Table 1. Photovoltaic Parameters of Different DSSCs Fabricated Using the 4, 6, and 8 h DSBS TiO_2 Nanostructures and P25 TiO_2 Nanoparticles[a]

sample	4 h	6 h	8 h	P25
length[b] (μm)	2	2.25	3	0
central[c] (μm)	3.5	3.3	3	6.5
length[d] (μm)	2	2.25	3	0
J_{sc}[e] (mA cm^{-2})	5.85	9.01	12.18	11.01
V_{oc}[f] (V)	0.76	0.79	0.78	0.76
FF[g]	65	58	59	50
η[h] (%)	2.89	4.12	5.61	4.18
f_p[i] (Hz)	5.9	10	17	26
τ[j] (ms)	27.1	15.9	8.3	6.1
R_s[k] (ohm)	10.7	11.1	5.8	11.8
R_1[l] (ohm)	19.5	12.5	11.6	19.6
R_2[m] (ohm)	544	176	161	57.7

[a]All measurements were made under AM 1.5 G full sunlight illumination (100 mW cm^{-2}). [b]Length of the top nanowries. [c]Thickness of the central nanoparticle layer. [d]Length of the bottom nanowries (as shown in Figure S10 in the Supporting Information). [e]Short-circuit current density. [f]Open circuit voltage. [g]Fill factor. [h]Light-electron conversion efficiency. [i]The minimum frequency on the Bode plot. [j]τ suggests a longer lifetime of electrons. [k]Sheet resistance. [l]Charge transfer resistance at the counter electrode/electrolyte interface. [m]Charge transfer resistance at the TiO_2/dye/electrolyte interface.

provided η = 5.6%, with J_{sc} = 12.18 mA cm^{-2}, V_{oc} = 0.78 V, and FF = 0.59. The results suggest that the microstructure of DSBS nanostructures, such as the length of nanowires, is one of the major factors that influences the device efficiency. For comparison, a solar cell assembled using P25 particles (0.25 cm^2, 6.5 μm thick nanoparticle layer) provided η = 4.18%, with J_{sc} = 11 mA cm^{-2}, V_{oc} = 0.76 V, and FF = 0.50.

As a control, a DSSC was assembled using only TiO_2 sol as the photoelectrode. The device characteristics measured from the I–V curve (see Figure S8 in the Supporting Information) were J_{sc} = 0.028 mA cm^{-2}, V_{oc} = 0.29 V, FF = 0.31, and η = 0.025%. The device performance was substantially inferior to those of DSBS TiO_2 /FTO-based DSSCs. Hence, the TiO_2 sol used as adhesive in the DSBS TiO_2-based DSSCs had a negligible contribution to the power conversion efficiency of the DSBS devices. The observed efficiency of DSSCs can be primarily attributed to the ordered DSBS TiO_2 /FTO glass photoelectrode for the backside illumination (see Figure S9a in the Supporting Information). The backside illumination enables light to effectively penetrate through the thin anatase layer, bottom nanowires, central nanoparticle layer, and top nanowires. The combination of the thin anatase layer and the central nanoparticle layer play an important role in avoiding light reflection as compared to frontside illumination (see Figure S9a in the Supporting Information) and conversional single-side nanowire arrays.[14,32] For confirmation, we have made measurements of the photocurrent-photovoltage characteristics for cells fabricated using the 8h DSBS TiO_2 nanostructure assembly under AM 1.5 illumination (100 mW cm^{-2}) from the frontside. As seen in Figure S9b in the Supporting Information, the backside illuminated cell shows better performance (η = 5.61%, with J_{sc} = 12.18 mA cm^{-2}, V_{oc} = 0.78 V, and FF = 0.59) as compared with the frontside illuminated cell (η = 5.13%, with J_{sc} = 12.00 mA cm^{-2}, V_{oc} = 0.75 V, and FF = 0.57).

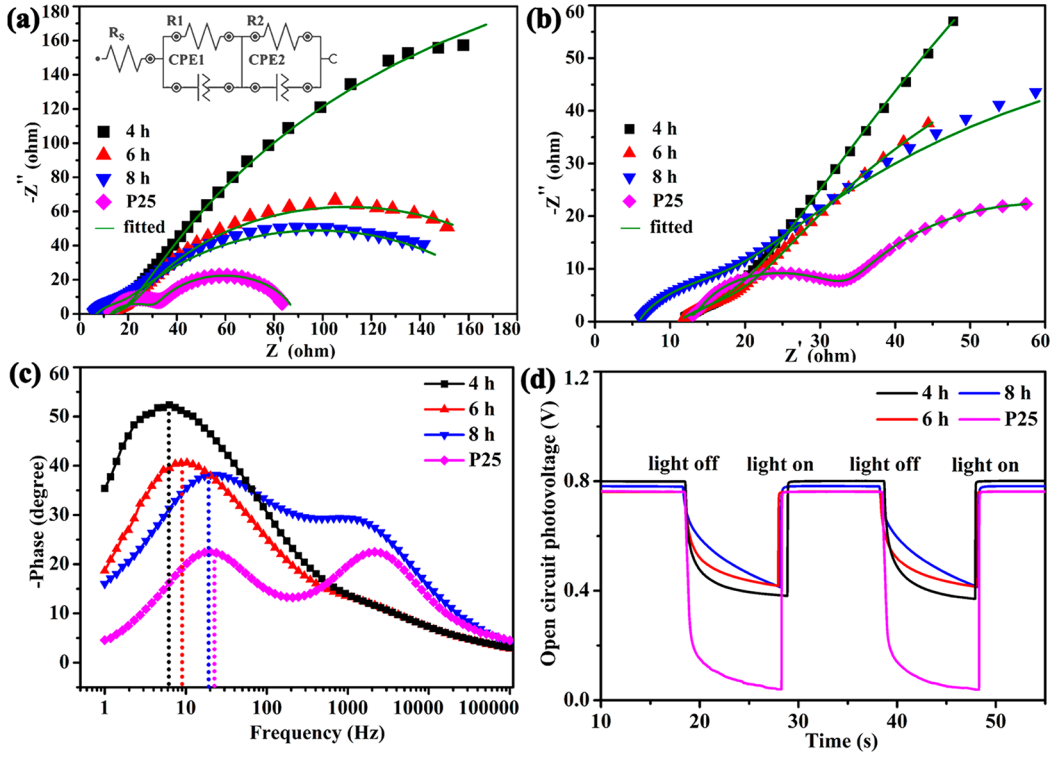

Figure 7. (a) Full scale (0–180 Ω) and (b) magnified (0–60 Ω) Nyquist plots, (c) Bode phase diagrams, and (d) photovoltage–decay measurements of the DSSCs fabricated using the 4, 6, and 8h DSBS TiO_2 nanostructures and P25 nanoparticles. The inset of Figure 7a shows the equivalent circuit used to obtain the fitted curves (solid lines) by fitting the experimental data (dots). All measurements were done under simulated AM1.5 solar light (100 mW cm^{-2}).

dx.doi.org/10.1021/am404942n | ACS Appl. Mater. Interfaces 2014, 6, 122–129

The initial structure of annealed P25 TiO_2 nanoparticle film layer is similar to that of nanoporous annealed P25 TiO_2 films used in conventional DSSCs. This annealed P25 TiO_2 nanoparticle film layer eventually became thinner with much larger internal space and less grain boundaries, as confirmed by the film's larger BET surface area of 60 m^2/g, due to continued dissolution of the anatase constituent (see Figure S10a, b in the Supporting Information). Thus, the center porous TiO_2 thin layer can improve the amount of dye loading within the DSBS structure as compared to conversional single-side nanowire structures. Moreover, the rutile phase of the annealed P25 TiO_2 nanoparticle layer acts as a seed for the growth of highly ordered lattice-matched rutile nanowires (See Figure S10c, d in the Supporting Information). The final DSBS structure can direct the transport of carriers through distances with resistance smaller than conventional TiO_2 nanoparticle agglomerates (see schematic illustration in Figure S11 in the Supporting Information).

The IPCE spectra of the devices fabricated using DSBS TiO_2 thin films with reaction time of 4 h, 6 h, 8 h, and for P25 nanoparticles are shown in Figure 6b. The device fabricated using the 8 h DSBS TiO_2 nanostructure shows the highest IPCE over the wavelength range of 350−700 nm. IPCE spectra of all the cells with N719 dye exhibited a maximum value at approximately 530 nm. As compared with the cell fabricated using P25 nanoparticles with similar thickness, the IPCE of the cell fabricated using the 8 h DSBS TiO_2 nanostructure shows the highest value over the entire wavelength region, which is consistent with its higher Jsc and efficiency as shown in Figure 6a.

Electrochemical impedance spectroscopy (EIS) was used to characterize the DSSCs fabricated using the 4, 6, and 8h DSBS TiO_2 thin films and P25 nanoparticles. Panels a and b in Figure 7 show full scale (0−180 Ω) and low-resistance scale (0-60 Ω) Nyquist-plots, respectively. An equivalent circuit (see the inset of Figure 7a) was used to fit the Nyquist plots to estimate the electron transport parameters, such as sheet resistance (R_S), charge transfer resistance at the counter electrode/electrolyte interface (R_1), and charge transfer resistance at the TiO_2/dye/electrolyte interface (R_2).[43] Equivalent circuits containing constant phase elements (CPE1 and CPE2) and resistances (R_1 and R_2) were used to fit respective resistances. As shown in Table 1, R_S, R_1, and R_2 of the nanowire-based DSSCs decrease with increasing of the length of nanowires. For the same cell, the resistance sequence is R_S<R1<R2. The R_S and R_1 values of the cell fabricated using the 8 h DSBS TiO_2 nanostructure is about half of those for the cell fabricated using P25 nanoparticles, whereas R_2 is about three times larger.

A further study using Bode phase-diagrams (Figure 7c) shows two well-defined semicircles in the high frequency (>1 kHz) and low frequency (1-1000 Hz) regions, representing the redox I^-/I_3^- reaction at the Pt/electrolyte interface and the electron transfer at the TiO_2/dye/electrolyte interface, respectively. The other invisible one at very low frequency (0.1−1 Hz) is attributed to the electron diffusion in I^-/I_3^- redox electrolytes. The lifetime of electrons in TiO_2 can be estimated from the following formula: $\tau = 1/(2\pi f_p)$.[44] Larger τ suggests that electrons have longer lifetime and faster diffusion rate in the nanowire film. f_p represents the minimum frequency that can enable the DSSC to achieve higher overall power conversion efficiency. As seen in Table 1, the lifetime of the electrons in the nanowire structures (27.1, 15.9, and 8.3 ms) is longer than that in the P25 nanoparticle film (6.1 ms) because of well-crystallized single-crystalline nature of the nanowires with less diffusive hindrance. The peak frequency at 1−100 Hz is inversely proportional to the electron lifetime.

Figure 7d and Figure S12 in the Supporting Information, respectively, shows the overall and the details of the initial photovoltage (V_{oc})−decay of the same four DSSCs. The electron recombination kinetics is investigated by monitoring the transient V_{oc} as a function of time after switching off the light. After the light is switched off with a shutter under a steady voltage, the Voc decays sharply due to electron recombination (see Figure S12 in the Supporting Information), which relates to the short electron lifetime. The nanowire-based DSSCs exhibit significantly slower Voc decay rates as compared to that of P25 nanoparticle-based DSSC. The longer electron lifetime indicates that more electrons can survive transport and thus improve the photocurrent and subsequent cell efficiency.

We have not tested the long-term performance stability of the cell after prolonged operation because the acetonitrile and valeronitrile in the electrolyte solution can etch the ionomer Surlyn 1702 used as glue to seal the cell. However, most of the chemicals and materials except for the TiO_2 nanostructure assembly have been widely used in reported DSSCs, and the long-term stability of well-sealed cells has been tested by other investigators. Thus, the present reported cell will likely be very stable after the sealing problem is addressed.

CONCLUSIONS

Double-sided brush-shaped TiO_2 nanostructures, with highly ordered vertically aligned nanowires, have been prepared under hydrothermal conditions using P25 nanoparticle powder coating acting as both the seed and providing structural support. The structural properties of the products including the crystalline phase, the phase composition, the length of the nanowires, and the thickness of the central nanoparticle layer can all be tuned by adjusting the hydrothermal reaction time. Backside illuminated dye-sensitized solar cells have been fabricated using the DSBS TiO_2 nanostructures. The cell efficiency is influenced by the microstructure, such as the length of the nanowires. Demonstrated conversion efficiency of 5.61% from a 8 h reaction time sample with 6 μm long nanowire arrays suggests that the synthesized DSBS TiO_2 nanostructures can be a very promising photoelectrode material for novel nanostructured solar cells.

ASSOCIATED CONTENT

Supporting Information

Digital photographs, nitrogen adsorption/desorption isotherms, XRD patterns, SEM images, photovoltaic parameters, $I-V$ curves, schematic diagrams, and photovoltage decay curves. This material is available free of charge via the Internet at http://pubs.acs.org.

AUTHOR INFORMATION

Corresponding Author

*E-mail: nzhbao@njut.edu.cn. Tel. & Fax: +86 25 83172244.

Notes

The authors declare no competing financial interest.

ACKNOWLEDGMENTS

This research was supported by the Natural Science Foundation of China (21006044, 51202110), the Natural Science Foundation of Jiangsu Province (BK2012426,

BK2012041), the Key Laboratory of Material-Oriented Chemical Engineering of China under Grant No. KL10-02, and the Project Funded by the Priority Academic Program Development of Jiangsu Higher Education Institutions (PAPD).

REFERENCES

(1) O'Regan, B.; Gratzel, M. *Nature* **1991**, *353*, 737−740.
(2) Gratzel, M. *Acc. Chem. Res.* **2009**, *42*, 1788−1798.
(3) Jose, R.; Thavasi, V.; Ramakrishna, S. *J. Am. Ceram. Soc.* **2009**, *92*, 289−301.
(4) Frank, A. J.; Kopidakis, N.; Lagemaat, J. V. D. *Coord. Chem. Rev.* **2004**, *248*, 1165−1179.
(5) Mor, G. K.; Shankar, K.; Paulose, M.; Varghese, O. K.; Grimes, C. A. *Nano Lett.* **2006**, *6*, 215−218.
(6) Ye, M. D.; Xin, X.; Lin, C.; Lin, Z. *Nano Lett.* **2011**, *11*, 3214−3220.
(7) Liu, B.; Aydil, E. S. *J. Am. Chem. Soc.* **2009**, *131*, 3985−3990.
(8) Law, M. L.; Greene, E.; Johnson, J. C.; Saykally, R.; Yang, P. D. *Nat. Mater.* **2005**, *4*, 455−459.
(9) Huang, Q.; Zhou, G.; Fang, L.; Hu, L.; Wang, Z. S. *Energy Environ. Sci.* **2011**, *4*, 2145−2151.
(10) Krishnamoorthy, T.; Thavasi, V.; Subodh, G. M.; Ramakrishna, S. *Energy Environ. Sci.* **2011**, *4*, 2807−2812.
(11) Shao, W.; Gu, F. L.; Gai, L.; Li, C. Z. *Chem. Commun.* **2011**, *47*, 5046−5048.
(12) Wei, X. F.; Liu, J. H.; Chua, Y. Z.; Song, J. L.; Liu, X. W. *Energy Environ. Sci.* **2011**, *4*, 2054−2057.
(13) Su, J.; Guo, L.; Bao, N.; Grimes, C. A. *Nano Lett.* **2011**, *11*, 1928−1933.
(14) Hore, S.; Vetterb, C.; Kern, R.; Smit, H.; Hinscha, A. *Sol. Energy Mater. Sol. Cells* **2006**, *90*, 1176−1188.
(15) Poudel, P.; Qiao, Q. *Nanoscale* **2012**, *4*, 2826−2838.
(16) Yella, A.; Lee, H. W.; Tsao, H. N.; Yi, C. Y.; Chandiran, A. K.; Nazeeruddin, M. K.; Diau, E. W. G.; Yeh, C.Y.; Zakeeruddin, S. M.; Gratzel, M. *Science* **2011**, *334*, 629−634.
(17) Liu, M.; Johnston, M. B.; Snaith, H. J. *Nature* **2013**, *501*, 395−8.
(18) Snaith, H. J.; Schmidt-Mende, L. *Adv. Mater.* **2007**, *19*, 3187−3200.
(19) Bavykin, D. V.; Friedrich, J. M.; Walsh, F. C. *Adv. Mater.* **2006**, *18*, 1−19.
(20) Leschkies, K. S.; Divakar, R.; Basu, J.; Enache-Pommer, E.; Boercker, J. E.; Carter, C. B.; Kortshagen, U. R.; Norris, D. J.; Aydil, E. S. *Nano Lett.* **2007**, *7*, 1793−1798.
(21) Mor, G. K.; Varghese, O. K.; Paulose, M.; Shankar, K.; Grimes, C. A. *Sol. Energy. Mater. Sol. Cells* **2006**, *90*, 2011−2075.
(22) Macak, J. M.; Tsuchiya, H.; Ghicov, A.; Yasuda, K.; Hahn, R.; Bauer, S.; Schmuki, P. *Curr. Opin. Solid State Mater. Sci.* **2007**, *11*, 3−18.
(23) Law, M.; Greene, L. E.; Johnson, J. C.; Saykally, R.; Yang, P. *Nat. Mater.* **2005**, *4*, 455−459.
(24) Zhang, Q.; Dandeneau, C. S.; Zhou, X.; Cao, G. *Adv. Mater.* **2009**, *21*, 4087−4108.
(25) Kakiuchi, K.; Hosono, E.; Imai, H.; Kimura, T.; Fujihara, S. *J. Cryst. Growth* **2006**, *293*, 541−545.
(26) Feng, X.; Zhu, K.; Frank, A. J.; Grimes, C. A.; Mallouk, T. E. *Angew. Chem. Int. Ed.* **2012**, *11*, 2727−2730.
(27) Sun, Z.; Kim, J. H.; Zhao, Y.; Attard, D.; Dou, S. X. *Chem. Commun.* **2013**, *10*, 966−998.
(28) Rawolle, M.; Niedermeier, M. A.; Kaune, G.; Perlich, J.; Lellig, P.; Memesa, M.; Cheng, Y. J.; Gutmann, J. S.; Müller-Buschbaum, P. *Chem. Soc, Rev.* **2012**, *41*, 5131−5142.
(29) Ito, S.; Kitamura, T.; Wada, Y.; Yanagida, S. *Sol. Energy. Mater. Sol. Cells* **2003**, *1*, 3−13.
(30) Kumar, A.; Madaria, A. R.; Zhou, C. W. *J. Phys. Chem. C* **2010**, *114*, 7787−7792.
(31) Hosono, E.; Fujihara, S.; Kakiuchi, K.; Imai, H. *J. Am. Chem. Soc.* **2004**, *126*, 7790−7791.
(32) Guldin, S.; Hüttner, S.; Kolle, M.; Welland, M. E.; Müller-Buschbaum, P.; Friend, R. H.; Steiner, U.; Tétreault, N. *Nano Lett.* **2010**, *10*, 2303−2309.
(33) Ito, S.; Zakeeruddin, S. M.; Humphry-Baker, R.; Liska, P.; Charvet, R.; Comte, P.; Nazeeruddin, M. K.; Péchy, P.; Takata, M.; Miura, H.; Uchida, S.; Gratzel, M. *Adv. Mater.* **2006**, *18*, 1202−1205.
(34) Ohsaka, T.; Izumi, F.; Fujiki, Y. *J. Raman Spectrosc.* **1978**, *7*, 321−324.
(35) Chaves, A.; Katiyan, K. S.; Porto, S. P. S. *Phys. Rev* **1974**, *10*, 3522−3533.
(36) Pottier, A.; Chanéac, C.; Tronc, E.; Mazerolles, L.; Jolivet, J. P. *J. Mater. Chem.* **2001**, *11*, 1161−1121.
(37) Orilall, M. C.; Wiesner, U. *Chem. Soc. Rev.* **2011**, *40*, 520−535.
(38) Yin, H. B.; Wada, Y.; Kitamura, T.; Kambe, S.; Murasawa, S.; Mori, H.; Sakata, T.; Yanagida, S. *J. Mater. Chem.* **2001**, *11*, 1694−1703.
(39) Shen, L.; Bao, N.; Zheng, Y.; Gupta, A.; Yanagisawa, K.; An, T. *J. Phys. Chem. C* **2008**, *24*, 8809−8818.
(40) Zheng, Y.; Shi, E.; Chen, Z.; Li, W.; Hu, X. *J. Mater. Chem.* **2001**, *11*, 1547−1551.
(41) Wu, H. B.; Hng, H. H.; Lou, X.W. *Adv. Mater.* **2012**, *19*, 2567−2571.
(42) Ambrus, Z.; Mogyorosi, K.; Szalai, A.; Alapi, T.; Demeter, K.; Dombi, A.; Sipos, P. *Appl. Catal., A* **2008**, *340*, 153−161.
(43) Wang, M.; Chen, P.; Humphry-Baker, R.; Zakeeruddin, S. M.; Gratzel, M. *Chem. Phys. Chem.* **2009**, *10*, 290−299.
(44) Song, D.; Kang, M. S.; Lee, Y. G.; Cho, W.; Lee, J. H.; Son, T.; Lee, K. J.; Nagarajan, S.; Sudhagar, P.; Yum, J. H.; Kang, Y. S. *Phys. Chem. Chem. Phys.* **2012**, *14*, 469−472.